AIDA-2020-PUB-2020-003

AIDA-2020

Advanced European Infrastructures for Detectors at Accelerators

Journal Publication

Performance of thin planar n-on-p silicon pixels after HL-LHC radiation uences

Ducourthial, A. (CNRS-LPNHE) *et al*

16 September 2019

The AIDA-2020 Advanced European Infrastructures for Detectors at Accelerators project has received funding from the European Union's Horizon 2020 Research and Innovation programme under Grant Agreement no. 654168.

This work is part of AIDA-2020 Work Package **7: Advanced hybrid pixel detectors**.

The electronic version of this AIDA-2020 Publication is available via the AIDA-2020 web site <http://aida2020.web.cern.ch> or on the CERN Document Server at the following URL: <http://cds.cern.ch/search?p=AIDA-2020-PUB-2020-003>

Performance of thin planar *n-on-p* silicon pixels after HL-LHC radiation fluences

A. DUCOURTHIAL[a], M. BOMBEN[a,*], G. CALDERINI[a], R. CAMACHO[a], L. D'ERAMO[a], I. LUISE[a], G. MARCHIORI[a], M. BOSCARDIN[b,c], L. BOSISIO[d], G. DARBO[e], G.-F. DALLA BETTA[c,f], G. GIACOMINI[g], M. MESCHINI[h], A. MESSINEO[i], S. RONCHIN[b,c], N. ZORZI[b,c]

[a] *LPNHE, Sorbonne Université, Paris Diderot Sorbonne Paris Cité, CNRS/IN2P3, Paris, France*
[b] *Fondazione Bruno Kessler, Centro per i Materiali e i Microsistemi (FBK-CMM) Povo di Trento (TN), Italy*
[c] *Trento Institute for Fundamental Physics and Applications (TIFPA INFN), Trento, Italy*
[d] *INFN Trieste, Trieste, Italy*
[e] *INFN Genova, Genova, Italy*
[f] *Università di Trento, Dipartimento di Ingegneria Industriale, I-38123 Trento, Italy*
[g] *Brookhaven National Laboratory, Instrumentation Division 535B, Upton, NY, U.S.A.*
[h] *INFN Firenze, Firenze, Italy*
[i] *Universita Pisa (IT), INFN Pisa, Pisa, Italy*

Abstract

The tracking detector of ATLAS, one of the experiments at the Large Hadron Collider (LHC), will be upgraded in 2024-2026 to cope with the challenging environment conditions of the High Luminosity LHC (HL-LHC). The LPNHE, in collaboration with FBK and INFN, has produced 130 μm thick $n-on-p$ silicon pixel sensors which can withstand the expected large particle fluences at HL-LHC, while delivering data at high rate with excellent hit efficiency. Such sensors were tested in beam before and after irradiation both at CERN-SPS and at DESY, and their performance are presented in this paper. Beam test data indicate that these detectors are suited for all the layers where planar sensors are foreseen in the future ATLAS tracker: hit-efficiency is greater than 97% for fluences of $\Phi \lesssim 7 \times 10^{15} \mathrm{n_{eq}/cm^2}$ and module power consumption is within the specified limits. Moreover, at a

*corresponding author

fluence of $\Phi = 1.3 \times 10^{16} \mathrm{n_{eq}/cm^2}$, hit-efficiency is still as high as 88% and charge collection efficiency is about 30%.

Keywords: Silicon Radiation Detectors, LHC, HL-LHC, Radiation Hardness

1. Introduction

CERN plans to upgrade the LHC into a high luminosity machine (High Luminosity LHC, HL-LHC) [1] to expand its physics reach. For this reason the ATLAS detector [2] will undergo a series of upgrades in the next years. In particular the ATLAS Inner Detector (ID, [3, 4]) will be replaced starting in 2024 by an all-Silicon system, the ATLAS Inner Tracker (ITk, [5, 6, 7]); data taking should resume in 2026. The new ATLAS tracking system will have to assure the same performance as the actual ID but in the much harsher environment of the HL-LHC. The upgraded LHC will deliver 5-7 times larger instantaneous luminosity, which translates into a similar increase of event pile-up, tracks density and radiation fluences/doses with respect to the LHC design values; the goal for HL-LHC is to deliver an integrated luminosity of 4000 $\mathrm{fb^{-1}}$ by 2037, after 10 years of operation [7]. The ATLAS ITk will include pixel detectors closest to the interaction point and micro-strip detectors at larger radii. The ITk Pixel Detector [7] will comprise 5 barrel layers and multiple rings to cover the very forward region, down to $|\eta| = 4$.[1]

The innermost pixel layers of ATLAS ITk are expected to integrate a radiation fluence Φ of 1-2$\times 10^{16}$ 1 MeV equivalent neutrons $(\mathrm{n_{eq}})/\mathrm{cm^2}$ by the end of 2037; this is a factor 4 larger than what the actual ATLAS Insertable B-Layer (IBL [8, 9]) is expected to have integrated by the end of 2023. Such a large increase in radiation fluence, with the request of a hit reconstruction efficiency of at least 97% [6] through the whole lifetime of the detector, dictates an activity of R&D toward thin pixel sensors in planar technology, with thicknesses of the order of 100-150 μm, to mitigate the impact of charge

[1] ATLAS uses a right-handed coordinate system with its origin at the nominal interaction point (IP) in the centre of the detector and the z-axis coinciding with the axis of the beam pipe. The x-axis points from the IP towards the centre of the LHC ring, and the y-axis points upward. Cylindrical coordinates (r,ϕ) are used in the transverse plane, ϕ being the azimuthal angle around the z-axis. The pseudorapidity is defined in terms of the polar angle θ as $\eta = -\ln\tan(\theta/2)$.

trapping from radiation damage induced defects. As a reminder, the ATLAS IBL planar sensors are 200 μm thick, while outer ATLAS Pixel detector layers feature 250 μm thick sensors. The main effect of such large radiation fluences will be the loss of collected signal, which can be as high as 70% for the largest HL-LHC fluences even for 200 μm thick detectors [8, 10].

In this paper we report on the beamtest performance of thin $n-on-p$ silicon pixel detectors aimed at the ATLAS ITk pixel innermost layers. In Section 2 the characteristics of the joint LPNHE/FBK/INFN pixel production will be presented, together with details of the irradiation campaign some detector modules from that production went through. After having discussed the beamlines used, the tracking telescope, and the data-acquisition, reconstruction and analysis software (Section 3), the beamtest results will be presented in Section 4. Conclusions will be drawn in Section 5.

2. LPNHE/FBK/INFN Thin Sensors Production and Irradiation Campaign

Thin $n-on-p$ planar pixel sensors have been realised at FBK[2] on high resistivity p-type 150 mm (6") wafers within the framework of the INFN Phase-2 program [11]. Si-Si Direct Wafer Bonded (DWB) wafers were chosen to fabricate pixel detectors; they are obtained by bonding together two different wafers: a high-resistivity (HR) Float Zone (FZ) sensor wafer and a low-resistivity (LR) Czochralski handle wafer. The FZ wafer is thinned to the desired thickness value, so as to obtain a wafer with a thin active layer plus a relatively thick mechanical support layer. P-type wafers of two different active depths (100 and 130 μm) with 500 μm thick handle wafers were used. The wafer layout included sensors compatible with one and two FE-I4 chip [12] modules (one chip module surface $\sim 20\times16.8$ mm^2), with pixel cell size of 50×250 μm^2. In Figure 1 a picture of one wafer from this production is shown. The ITk Pixel Detector modules will be equipped with a completely new readout chip; a first prototype, the RD53A [13], was recently produced. The pixel cell size is of 50×50 μm^2; it can be used to readout a sensor with pixel cells of the same size but also the 25×100 μm^2 option is currently being explored.

Permanent biasing structures were implemented on the pixel sensors, consisting of a small circular n^+ implant (*bias dot*) in the corner between four

[2]FBK-CMM (Trento, Italy): `http://cmm.fbk.eu/`

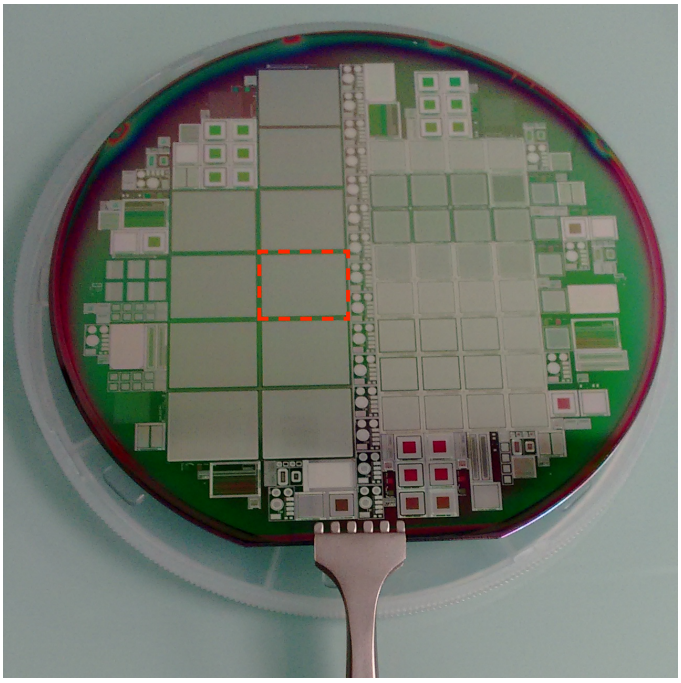

Figure 1: Wafer from the $n-on-p$ planar technology production [11] whose layout was mainly based on ATLAS FE-I4 and CMS PSI46 [14] designs. The red rectangle encircles one pixel sensor compatible with the FE-I4 readout chip.

neighbouring pixel cells; all bias dots were shorted together through a metal line (*bias lane*). Thanks to these structures, by exploiting the punch-through mechanism, the pixels could be tested electrically before bump-bonding to the readout chips. In Figure 2 a scheme of the pixels cells. The diameter of the implant of the bias dot is of 27 μm; the metallization diameter is 4 μm smaller. The pixel implant is 37 μm high and about 200 μm long; the metallization of the pixel cell is about 3 μm shorter on both sides. As a comparison in Figure 2 a scheme of pixel cells from a previous production [15] is shown, where the temporary metal solution [16] was used to bias the sensor before bump-bonding. In this case the pixel implant is 27 μm high and about 220 μm wide. The pixel metallization is 4 μm wider than the implant.

2.1. Pixel module irradiation

Radiation hardness was tested by measuring the performance of irradiated pixel sensors connected to FE-I4 readout chips. Two sensors, named *W80* and *W30*, were taken from two different sensor wafers, with thickness of 130

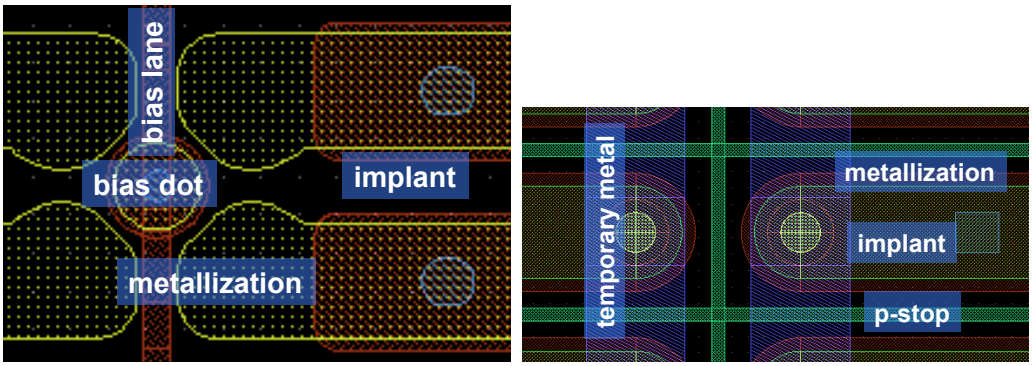

Figure 2: (left) Schematic view of parts of pixel cells presented in this article. The salient parts are indicated. (right) The scheme of pixels cell from a previous production [15] is reported, where temporary metal lanes where used for biasing before bump-bonding.

(100) μm for W80 (W30); the sensors had different number of guard rings (GRs), 2 and 5, respectively. Sensors details are summarised in Table 1. In both detector assemblies the 500 μm thick handle wafer was not thinned. A Benzo-Cyclo-Butene (BCB) layer was deposited on the sensors for spark protection (for more details [17, 18]). Each sensor was bump bonded to an FE-I4 chip at IZM, Berlin[3].

The irradiations of W80 and W30 were carried at room temperature at the CERN IRRAD facility[4] using a 24 GeV/c proton beam. For both pixel modules the irradiation was staged in two steps. Table 1 gives the details of the irradiation program for the two modules tested from that production, W80 and W30; their characteristics are reported too. It has to be noted that the IRRAD beam profile is gaussian with FWHM ranging from 12 to 20 mm.

In summary W80 (W30) received during the first irradiation experiment an average fluence ϕ of about 3 (4) $\times 10^{15}$ n_{eq}/cm^2 and of 7 (7)$\times 10^{15}$ n_{eq}/cm^2 during the second irradiation experiment; after the second irradiation experiment the average cumulative fluence Φ received by W80 (W30) was of about 1.0 (1.1)$\times 10^{16}$ n_{eq}/cm^2.

At the IRRAD facility several beam position monitors (BPMs), which register the beam intensity during the irradiation along the horizontal and

[3]Fraunhofer-Institut für Zuverlässigkeit und Microintegration: `https://www.izm.fraunhofer.de/en.html`

[4]`http://ps-irrad.web.cern.ch/`

Table 1: Irradiation program for the two FE-I4 pixel modules W80 and W30. For both pixel modules the irradiation was staged in two steps; the average fluence ϕ is reported for each step. The average cumulative fluence Φ after the second step is reported too.

Module name (thickness [μm], # of GRs)	Beam spot size (FWHM - [mm^2])	<Fluence> ϕ [10^{15} n_{eq}/cm^2]	<Cumulative fluence> Φ [10^{15} n_{eq}/cm^2]
W80 (130, 2)	20×20	3	3
W30 (100, 5)	12×12	4	4
W80 (130, 2)	20×20	7	10
W30 (100, 5)	20×20	7	11

vertical direction orthogonal to the beam, allow reconstructing the beam profile. The accuracy in the position determination is of the order of 2 mm, which includes the different sources of misalignment. Figure 3 shows the beam profile intensity projected along the horizontal and vertical direction; the two projections have been fitted with a gaussian to determine the center position and the beam widths. It can be seen that the center vertical position

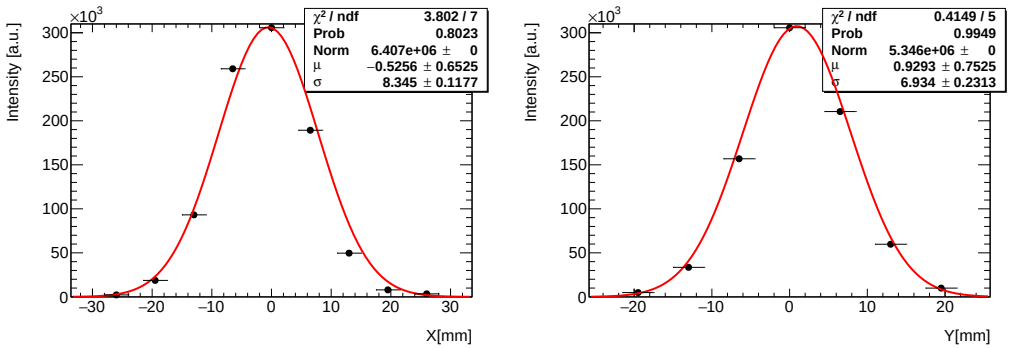

Figure 3: Projections of the proton beam profile used at CERN IRRAD to irradiate the W80 module. Left: horizontal direction; right: vertical direction. A gaussian fit is superimposed. The (0,0) position correspond to the nominal beam center.

is not compatible with $y = 0$; this has been confirmed by the IRRAD facility managers.

The dosimetry information made possible to estimate the total delivered proton fluence, transformed then into n_{eq}/cm^2 using an hardness factor $\kappa = 0.59$, with an uncertainty of about 10%. In Figure 4 the fluence profile after the second irradiation step is reported for the W80 module. It can be seen that the highest fluence is about $\Phi = 1.4 \times 10^{16}$ n_{eq}/cm^2, while at the detector

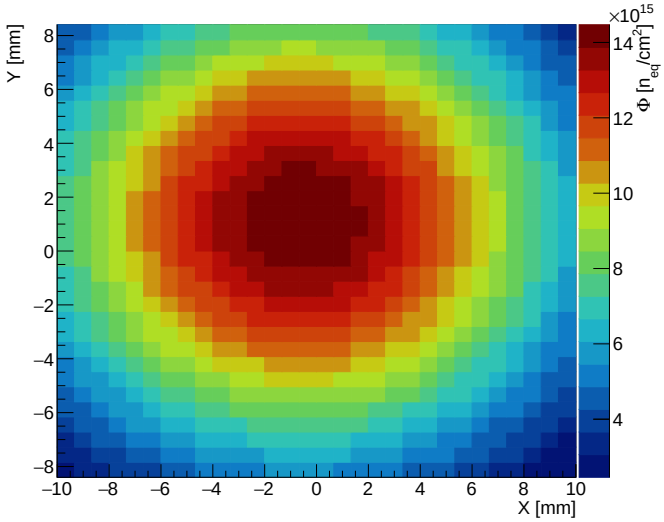

Figure 4: Fluence profile for W80 module after the the second irradiation step. The area covered by the figure corresponds to the surface of the W80 pixel module.

periphery the fluence is as low as $\Phi = 3.5 \times 10^{15}$ n_{eq}/cm^2. Thanks to the high segmentation of the pixel detector modules it was then possible to probe several fluences over a large range of values with just one pixel detector.

2.2. Electrical Performance after Irradiation

In what follows the pixel sensor leakage current and power consumption performance are presented as a function of the bias voltage. The average cumulative fluence Φ from Table 1 is used as a measure of the irradiation fluence received by the module itself[5]. The leakage current as a function of the bias voltage for different fluences and at different temperatures is reported in Figure 5 for the W80 pixel module after irradiation.

The trend of the leakage as of function of bias voltage for the largest fluence seems compatible with a convex function, while the one for the lowest fluence looks more like a concave function. One possible explanation for the trend at large fluence is the onset of impact ionisation, leading to current multiplication.

[5]The leakage current per pixel cell was not recorded; only the leakage current of the whole module is available

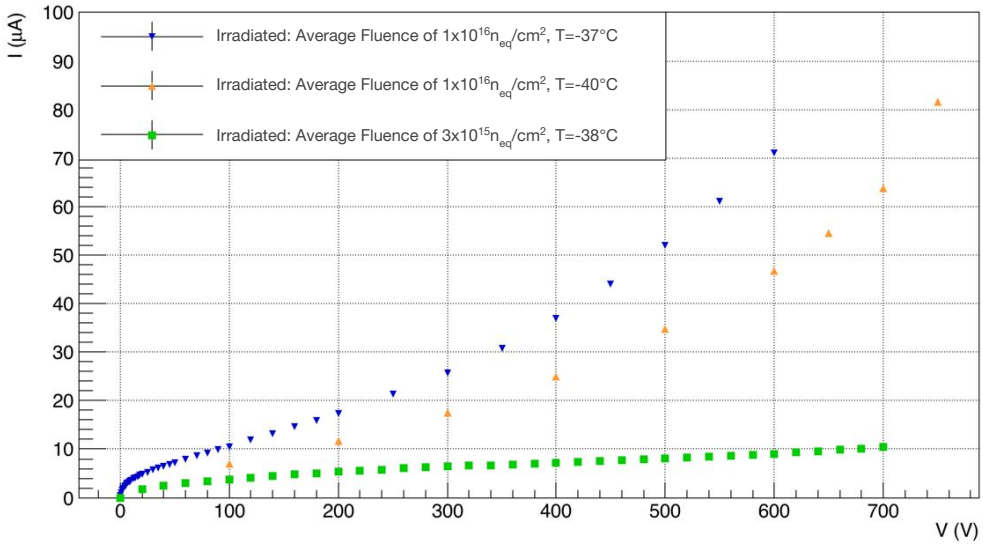

Figure 5: Current-Voltage curves of W80 sensor after a fluence of $3 \times 10^{15}\,\mathrm{n_{eq}/cm^2}$ (green markers) and after a cumulative fluence of $1 \times 10^{16}\,\mathrm{n_{eq}/cm^2}$ (blue and yellow markers). The temperature at which the measurements were taken is indicated in the legend.

The increase of leakage current I with the fluence Φ is expected to be linear: $\Delta I = \alpha V \Phi$, where $\alpha \sim 4 \times 10^{-17}$A/cm is the so-called *current related damage rate* [19] and V is the volume of the sensor. The data reported in Figure 5 were used to extract the current related damage rate α at $V_{bias} = 600$ V after rescaling the current to $t = 20°$ C. The leakage current was rescaled according to the formula of Ref. [20] ($I(T) \sim T^2 \exp(-E_{eff}/(2k_BT))$ with two E_{eff} values, *i.e.* 1.12 and 1.21 eV; two E_{eff} values were considered because recent measurements[6] favour a value for E_{eff} close to the energy gap E_g.

As it can be seen in Table 2, for all fluences, temperatures and E_{eff} values the current related damage rate α values are in the correct ballpark. The two results for the largest fluence at two slightly different temperatures are in good agreement, which indicates the reproducibility of the method.
From Table 2 it can be seen that the value of α for the largest fluence can be as high as twice the "standard value" (4×10^{-17}A/cm). This result, together with the fact that the leakage current curve is compatible with a

[6]MPG ATLAS group, private communication

Table 2: Current related damage rate α values for W80 sensors at V_{bias} = 600 V for two fluences and different temperatures. The uncertainty on the values is due to the temperature uncertainty of 1° C.

	α (10^{-17}A/cm)	
	E_{eff} = 1.12 eV	E_{eff} = 1.21 eV
$\Phi = 3 \times 10^{15} \mathrm{n_{eq}/cm^2}$, t = -38° C	2.6 ± 0.4	4.0 ± 0.6
$\Phi = 1 \times 10^{16} \mathrm{n_{eq}/cm^2}$, t = -40° C	5.2 ± 0.7	8.2 ± 1.2
$\Phi = 1 \times 10^{16} \mathrm{n_{eq}/cm^2}$, t = -37° C	5.3 ± 0.7	8.2 ± 1.2

convex function, might be a strong argument in favour of the onset of impact ionisation. It has to be anyhow noted that pixel modules did not undergo the "standard" annealing of 80 minutes at 60° C (they were kept cold most of the time after irradiation and they were always measured at below 0° C temperature[7]); hence it cannot be ruled out a contribution to the leakage current to non-annealed defects [19].

In Figure 6 the power dissipation per unit area of the W80 detector after irradiation is reported as a function of bias voltage, for different fluences and temperatures; the power dissipation was computed as the product of leakage current times bias voltage.

At a bias voltage of 600 V the power dissipation per unit area is about 6 mW/cm^2 after a fluence of 3×10^{15} n$_{\mathrm{eq}}$/cm^2 when scaled to $t = -25°$ C (the expected pixel detector temperature at ITk [7]) using the same formula used for the leakage current; this power dissipation is just below the specification for ITk pixels at $\Phi = 2 \times 10^{15}$ n$_{\mathrm{eq}}$/cm^2 (6.4 mW/cm^2 [7]). At $\Phi = 1 \times 10^{16}$ n$_{\mathrm{eq}}$/cm^2 the power dissipation is about 40 mW/cm^2; this value is comparable to what has been reported in [21] for 100 μm thick pixel detectors aimed at ITk.

[7]They spent some unknown amount of time at room temperature after irradiation at IRRAD facility

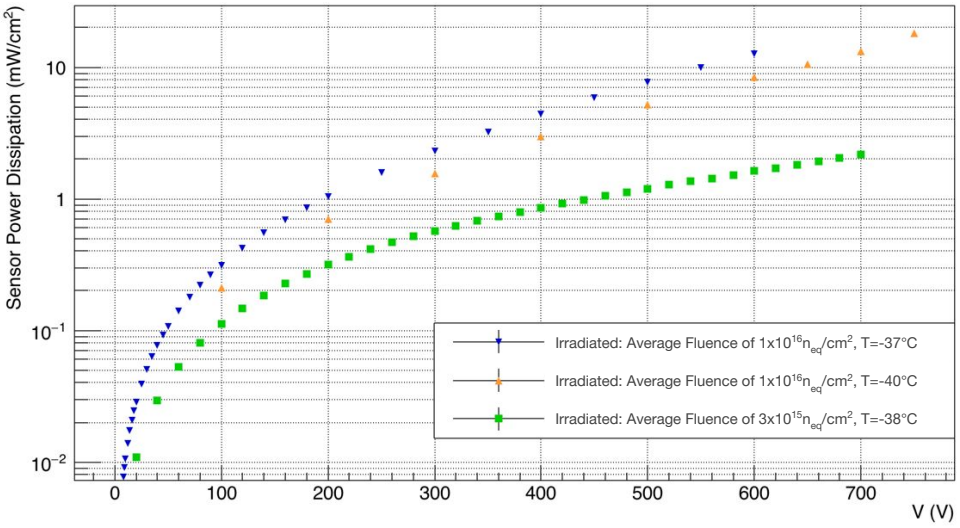

Figure 6: Sensor power dissipation curves of W80 sensor after a fluence of $\Phi = 3 \times 10^{15} \mathrm{n_{eq}/cm^2}$ (green markers) and after a fluence of $\Phi = 1 \times 10^{16} \mathrm{n_{eq}/cm^2}$ (blue and yellow markers). The temperature is indicated in the legend.

3. Testbeam Data Taking

Measurements reported here were carried out in 2017 and 2018 at the DESY beam test facility [8] and at the CERN-SPS experimental area [9], using copies of the EUDET/AIDA telescope [22]. At DESY, 4 GeV/c electrons from an almost continuous beam were used. At CERN, 120 GeV/c positive pions were used. The time structure of the beam was organised in spills within a super cycle of several tens of seconds. In what follows a summary of the experimental conditions will be given; more details of the testbeam facilities, tracking telescopes, data acquisition system, reconstruction and analysis software used can be found in Refs. [15] and [23].

The devices under test (DUTs) were mounted between the two arms of the tracking telescope. Each telescope arm comprised three Mimosa26 [24] sensing planes. Each Mimosa26 sensor matrix is composed by 576×1152 pixels of 18.4 μm pitch. During the measurements the DUTs were housed in

[8] http://testbeam.desy.de/
[9] http://sba.web.cern.ch/sba/

a cooling box which assured the DUTs were at controlled temperature (down to -50° C) and protected from light. Data acquisition was triggered by the coincidence signal of two plastic scintillators, whose overlap area was about 1 cm^2.

Prior to data taking, the DUTs were carefully tuned to choose a threshold value and the correspondence between the Time-over-Threshold (ToT) [12] value and input charge is calibrated. In our DUTs, the signal generated by a MIP[10] traversing the sensor is digitized into a 4 bit ToT register. The threshold is chosen to assure high signal efficiency while minimising the noise. For our thin sensors (100-130 μm thickness) thresholds ranging between 700 e and 1200 e were chosen. Once a threshold is selected, a ToT-to-charge calibration has to be performed: a ToT value will be related to a corresponding amount of charge induced on the electrodes. Usually this calibration is tuned to match ToT values in the middle of the dynamic range of the 4-bit register (5-8) to the expected signal of a MIP in the sensor. For example, in 130 μm thick sensors, a MIP is expected to generate about 10 ke, hence a typical ToT tuning for such a detector would be 5 ToT for a signal of 10 ke. After irradiation, as charge carriers are trapped, the signal amplitude decreases and a lower charge per ToT unit is better suited, such as 6 ToT for a signal of 6 ke.

4. Testbeam results

In this section the testbeam results will be presented after a discussion of the corrections applied to the fluence map (Sections 4.1 and 4.2) presented in Section 2.1. Data presented in this section were reconstructed using EUtelescope [25] and analysed using the TBmon2 [26] framework.

4.1. Corrections to Fluence Map

The fluence maps of W80 have been presented in Section 2.1. From dosimetry results, the fluence beam profile (see Figure 4) can be modeled by 2D gaussians, with a 2 mm uncertainty on the position in both X and Y directions. To further constrain the fluence peak position and reduce the uncertainties on this position, the mean cluster ToT distribution across the sensor was used. As the charge trapping effect increases with the fluence, the collected charge and consequently the ToT are also reduced. Hence the position

[10]Minimum Ionising Particle

of the minimum of the mean ToT distribution of a cluster is a valid indicator of the fluence peak position. For this purpose, various configurations in terms of threshold, ToT configuration and bias voltage have been investigated, as reported in Table 3

Table 3: Summary of the various configurations investigated for W80 after the second irradiation step. The ToT tuning describes the ToT value corresponding to a charge collected by the electrode. The charge target value (in units of thousand of electrons) is indicated by i.

Threshold [electrons]	850	850	850	1000	1000	1200
ToT at i ke-	8 at 4	8 at 4	8 at 4	8 at 4	6 at 4	6 at 4
Bias Voltage [V]	600	500	400	600	600	600

The search of the irradiation beam profile position has been performed with data taken at DESY where the beam profile was wider than what it was at CERN-SPS. During this testbeam two ROI (Regions Of Interest) have been considered which area were covered by the beam with a sufficient amount of statistics (the edges of the beam profiles where the statistics is too limited are not considered). The ROI covering the lower part of the sensor will be referred as "Down" position in the following; the other covering the upper-medium part of the sensor will be referred as "Up" position in the following[11]. Both ROIs are presented in Figure 7

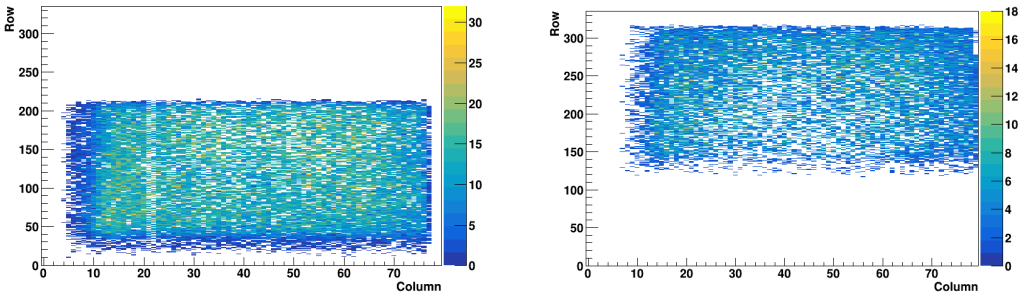

Figure 7: Hit map of W80. The Down and Up ROI are visible respectively in the left and right plots.

Two profiles have been created, an horizontal profile which averages all the mean ToT values of each pixel along the vertical axis in the ROI and a

[11]The choice of the regions was dictated by the triggering scintillators coverage

vertical profile which averages all the mean ToT values of each pixel along the horizontal axis in the ROI. To obtain the value of the peak fluence position, the average ToT profiles have been created for all the configurations from Table 3 and they are presented in Figure 8.

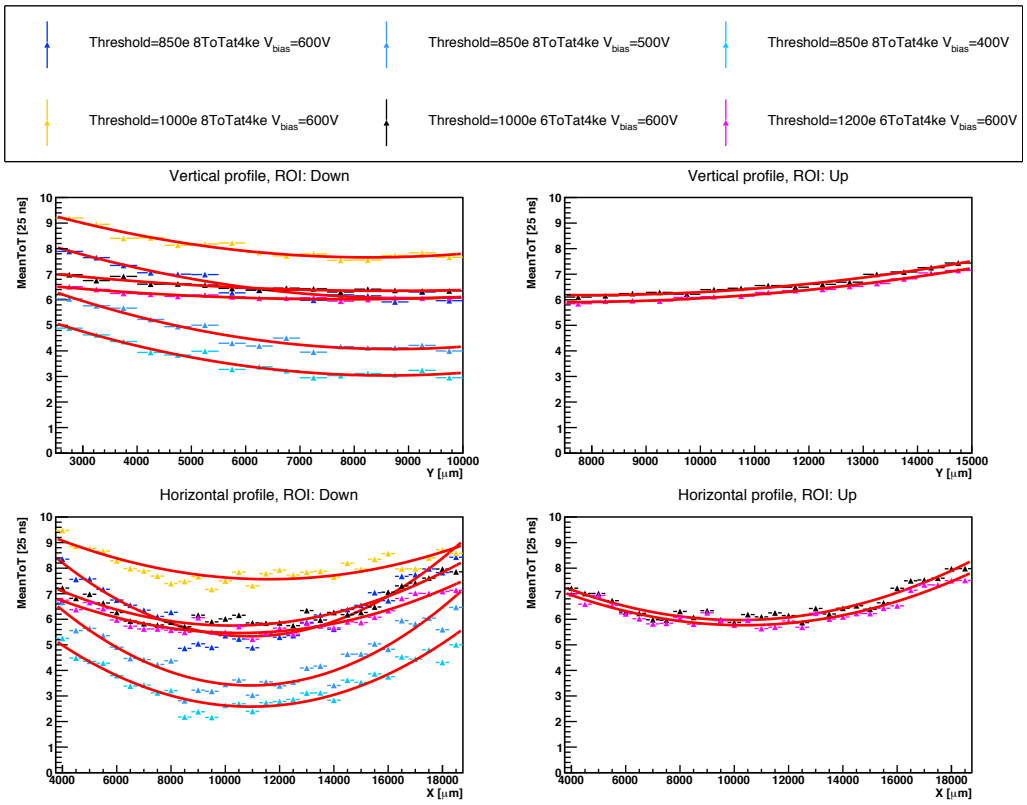

Figure 8: Average ToT profiles for the two ROI. The threshold, ToT tuning and bias voltage are indicated in the legend box. Each distribution is fitted with a polynomial of degree two (red lines).

Each distribution is fitted with a 2^{nd} degree polynomial and the minimum of the distribution is extracted from the fit. The mean of the average ToT minimum position value, which corresponds to the fluence peak position, is obtained by averaging the extracted values of all configurations. The fluence peak position estimated in this way is shifted by 1.2 mm in X and by 1 mm in Y with respect to the position presented in Section 2.1; the shift is within the 2 mm uncertainty on the position indicated by the CERN IRRAD facility.

The effect of the modification of the peak fluence is presented in Figure 9

which shows the average ToT vs fluence for 3 different bias voltages without (left plot) and with (right plot) fluence peak constraint. The constraint of the fluence peak (right plot) results in less dispersion in the average ToT values for the same fluence.

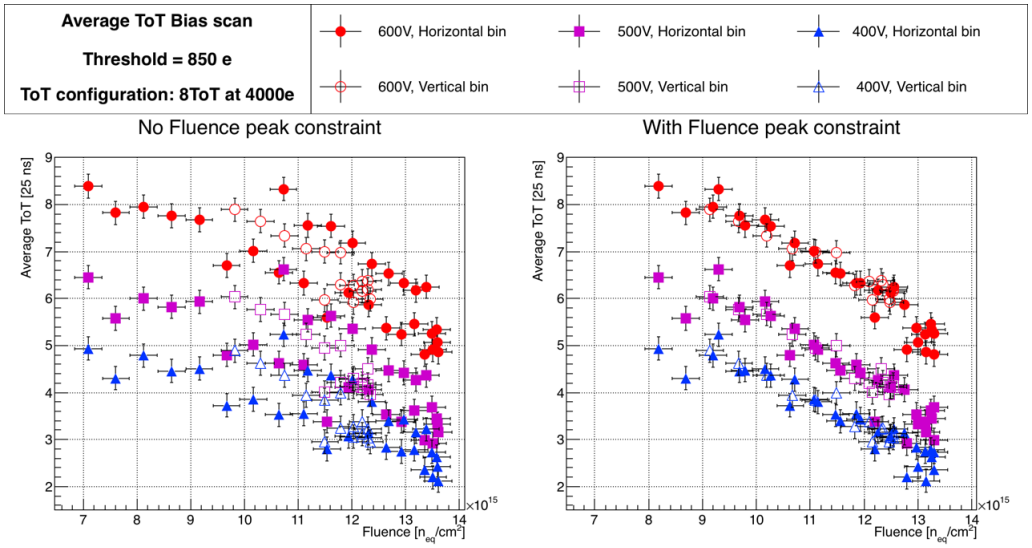

Figure 9: Average ToT distribution vs fluence for three different bias voltages. The left/right plot is without/with fluence peak constraint. The horizontal/vertical bin label in the legend means that the fluence and average ToT have been extracted from an horizontal/vertical profile of the Down ROI.

The uncertainty on the fluence in Figure 9 is set to $0.5 \times 10^{15} \mathrm{n_{eq}/cm^2}$, which corresponds to the variation of the fluence at 2 mm of the peak value. It accounts for the uncertainty on the peak fluence and on the fluence profile modelling approximation.

4.2. Other Systematic Effects on Fluence Determination

Even if the constraint on the fluence peak shows better results in terms of dispersion, some other effects have to be accounted for. The average ToT distribution is highly sensitive to the chosen threshold and ToT value, as well as to the bias voltage. As several tunings have been investigated and give consistent results with respect to one another, the peak fluence position is assumed rather independent of the tuning. Another effect is the non uniformity of the threshold across the different pixels observed in the FEI4 chip. This has an impact on the average ToT, as presented in Figure 10,

which shows the average ToT distribution on the un-irradiated reference DUT used in the testbeam where the previous data were extracted. A variation of

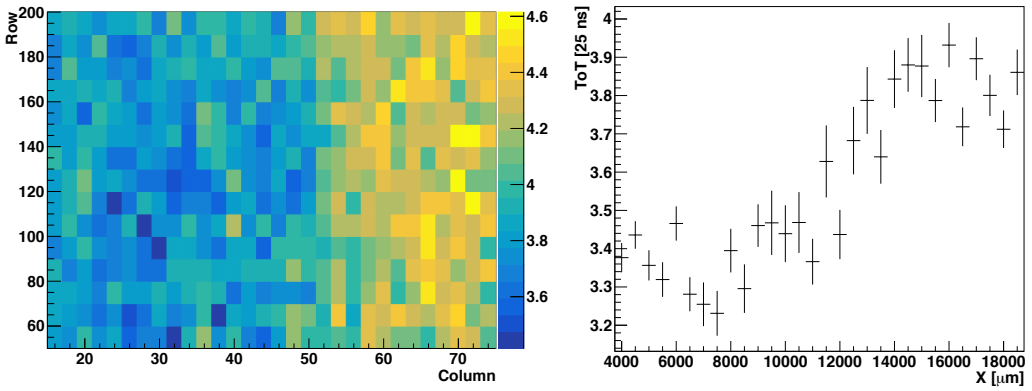

(a) MeanToT map of reference DUT

(b) Horizontal profile

Figure 10: Cluster ToT map (a) and ToT horizontal profiles for the reference DUT (un-irradiated). The DUT tuning was 4 ToT at 8 ke-.

the average ToT of about 0.5 ToT can be seen across the sensor even if this sensor was un-irradiated. The difference in ToT occurs mainly horizontally. This ToT variation can be explained by a drift in the threshold already seen by other users of FEI4 modules[12]. To take into account this effect, which is difficult to quantify from one chip to another, a conservative systematic uncertainty of 0.5 ToT was assigned to the ToT value .

4.3. Hit Efficiency

The hit efficiency ϵ, defined as the fraction of reconstructed tracks crossing a module that have an associated hit in that module, was studied as a function of the irradiation fluence Φ using data collected at DESY testbeam facility, and contrasted with a result for an un-irradiated dectector. The results are presented in Figure 11.

The efficiency versus fluence measurements of the two irradiation steps were fitted with a straight line. The horizontal uncertainty bars account for the uncertainty on the fluence peak position and on the modelling of the irradiation profiles, as explained in Section 4.1 and 4.2. The vertical

[12]MPG ATLAS group, private communication

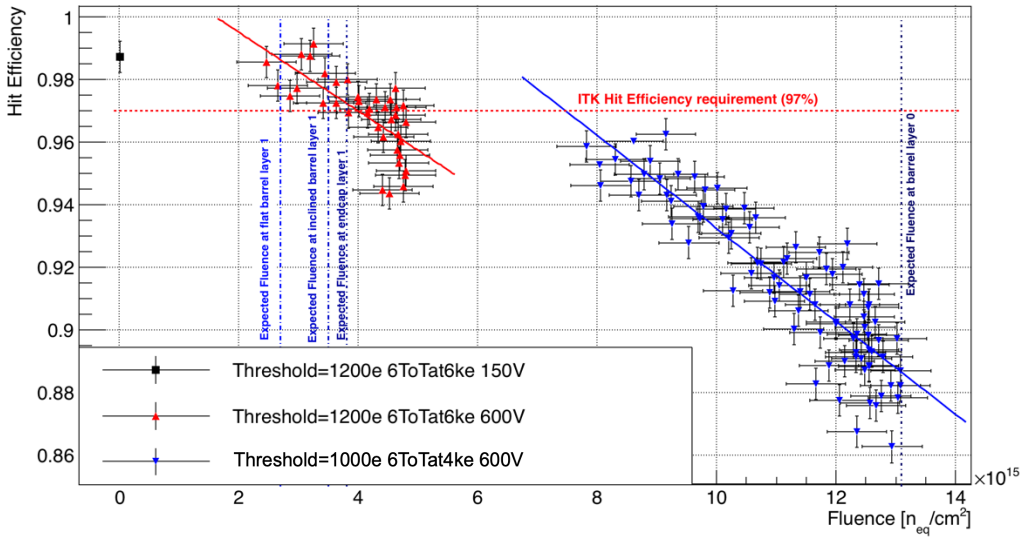

Figure 11: Hit efficiency for a 130 μm thick sensor at various irradiation fluences. The blue triangles are for sensor irradiated at $\Phi = 1 \times 10^{16} \mathrm{n_{eq}/cm^2}$ and the red ones at $\Phi = 3 \times 10^{15} \mathrm{n_{eq}/cm^2}$. The black square represents data for a thin un irradiated sensor. Threshold, ToT calibration and bias voltage are indicated.

error bars are the combination of the systematic uncertainties arising from the selection criteria variations (0.4%) and from the statistical fluctuations (0.25%). For the statistical part, for all fluence points at least 5000 tracks were considered, hence the statistical (binomial) error is less than 0.25%. The horizontal red dotted line represents the hit efficiency requirements of the ITk (97%) [7]. The four vertical blue dotted lines correspond the limit fluence expected at the end of lifetime of four different layers of ITk. From lower to higher fluences one can find [7]:

- the fluence expected ($\Phi = 2.7 \times 10^{15} \mathrm{n_{eq}/cm^2}$) at the layer 1 (second layer from the beam pipe) in the central (barrel) flat part;
- the fluence expected ($\Phi = 3.5 \times 10^{15} \mathrm{n_{eq}/cm^2}$) at the layer 1 in the inclined part of the barrel;
- the fluence expected ($\Phi = 3.8 \times 10^{15} \mathrm{n_{eq}/cm^2}$) at the layer 1 in the endcap part;
- the fluence expected ($\Phi = 1.3 \times 10^{16} \mathrm{n_{eq}/cm^2}$) at the layer 0 (closest layer to the beam pipe) in the flat barrel part.

Table 4: Extrapolated efficiency for ITk benchmarks fluences for a 130 μm thick sensor.

Fluence ($\Phi = 1 \times 10^{15} n_{eq}/cm^2$)	2.7	3.5	3.8	7.45	13.1
Threshold (electrons)	1200	1200	1200	1000	1000
ToT tuning (ToT corresponding to ke-)	6 at 6	6 at 6	6 at 6	6 at 4	6 at 4
Extrapolated Hit Efficiency (%)	98.6	97.6	97.2	97.0	88.6

Table 4 presents the expected efficiency for the various fluences, obtained from the crossing point of the fit and the fluence lines. The fluence ($\sim 7.45 \times 10^{15} n_{eq}/cm^2$) at which the hit efficiency is 97% is reported too.

The measured efficiency obtained for the fluences of the various layer 1 parts are all above the 97% requirement. A lower threshold and a better tuning could certainly help to reach higher values in terms of efficiency. For example, the prediction from the 1000e threshold data, assuming a linear dependency shows that the crossing between the ITk requirement line and the extrapolated values happen around $\Phi = 7 \times 10^{15} n_{eq}/cm^2$. As a reminder, pixels detectors in 3D technology [27] are the baseline for the innermost layer of the ITk Pixels detector; those pixels modules will be replaced at half-life of the HL-LHC, after an integrated luminosity of about 2000 fb^{-1}.

4.4. Pixel Resolved Hit Efficiency

In Figure 12 the hit efficiency for two different pixel detectors in several conditions is reported after having folded all cells in the matrix into one - the so-called *pixel resolved hit efficiency*[13]. Data are presented for three different fluences; unirradiated, and irradiated with a fluence of $\Phi = 3 \times 10^{15} n_{eq}/cm^2$ and of $\Phi = 1 \times 10^{16} n_{eq}/cm^2$. As indicated in Section 1 the W80 pixel sensor featured permanent biasing structure exploiting the *punch through* mechanism. The punch through structure clearly degrades the performance at the corner of the sensor cell. This is already evident before irradiation, especially when the pixel resolved hit efficiency is to compared to the case where no permanent biasing structures are present (left column of the Figure; data from Ref. [15]).

[13]This analysis is possible thanks to the good pointing resolution of the tracks telescope, even with the low energy beam of DESY.

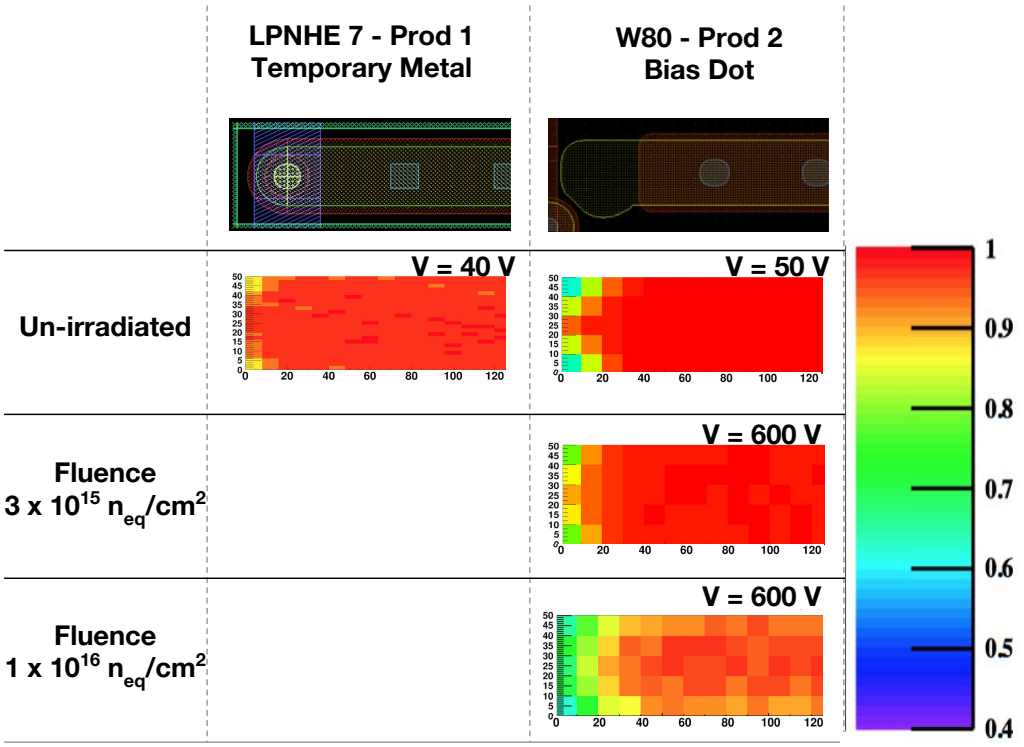

Figure 12: Pixel resolved hit efficiency for two pixel sensors: left one from [15], right one is W80. Results are presented for 3 different fluences for the W80; the corresponding sensor bias voltage is indicated. A scheme of the pixel is presented in the top part of the figure. See Section 2 and in particular Figure 2 and for details about the pixel cells parts.

4.5. Charge Collection Performance

Charge collection performance was studied as a function of fluence and bias voltage for W80 module.

Charge Collection vs Bias Voltage. The analysis started looking at cluster ToT evolution with bias voltage for the W80 module after the second step of irradiation. Data were taken at CERN and the level of beam collimation did not allow us to do the detailed fluence analysis proposed for data taken at DESY. Hence the fluence is averaged over the illuminated area. The tested configurations had a threshold of 850 electrons and the ToT to charge calibration was 8 ToT for 4000 electrons. All the distributions were fitted with a Landau distribution convoluted with a Gaussian resolution function allowing

the determination of the Most Probable Value (MPV) [28]. In Figure 13 it can be seen that at high fluences the cluster ToT MPV increases linearly with the bias voltage in the range between 400 V and 600 V. At 400 V the

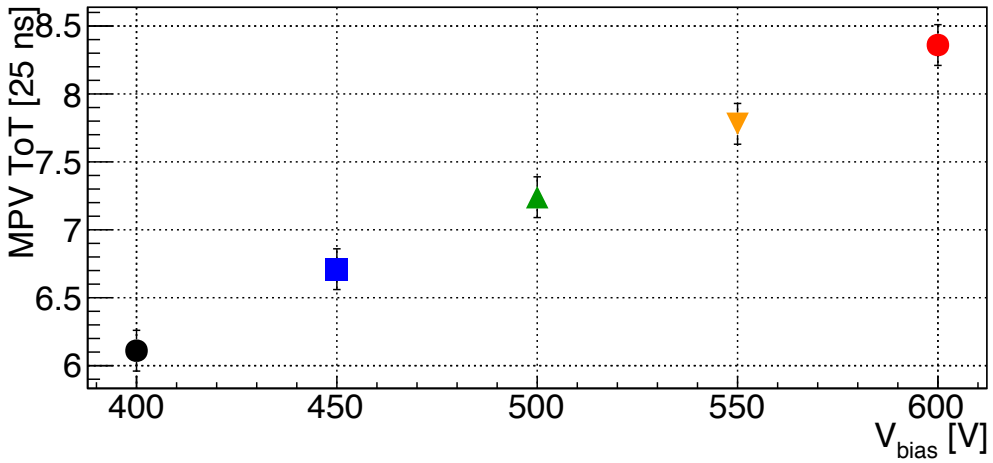

Figure 13: ToT distribution for thin sensor irradiated at $\Phi = 1 \times 10^{16} \mathrm{n_{eq}/cm^2}$ (from [28]).

MPV is 73% of the one at 600 V. At 600V the ToT MPV is $\simeq 8.5$, which corresponds to a charge slightly higher than 4000 electrons. By comparison with unirradiated sensor, this means that the collection efficiency is roughly reduced by a factor of 2 after an irradiation at $\Phi = 1 \times 10^{16} \mathrm{n_{eq}/cm^2}$.

Charge Collection Efficiency vs Fluence. Using the data collected at DESY - thanks to the wide beam spot - it was possible to investigate charge collection all over the pixel matrix and hence extract the charge collection performance as a function of the irradiation fluence. ToT to Charge calibrations were performed using STControl [29] software.

The collected charge for the irradiated W80 module and for the un-irradiated W30 module is plotted in Figure 14.

This plot compiles results from 3 testbeams where the W30 sensor was tested un-irradiated, biased at 150 V and with a threshold of 1200e and a ToT configuration of 6ToT corresponding to 6000 electrons (black square on the plot), and W80 sensor was tested after the first irradiation step (red triangles) and after the second irradiation step (blue triangles). Before irradiation, the mean collected charge is 12500 electrons which is quite close to what is expected for a 100 μm thick sensor. The decrease with fluence of collected

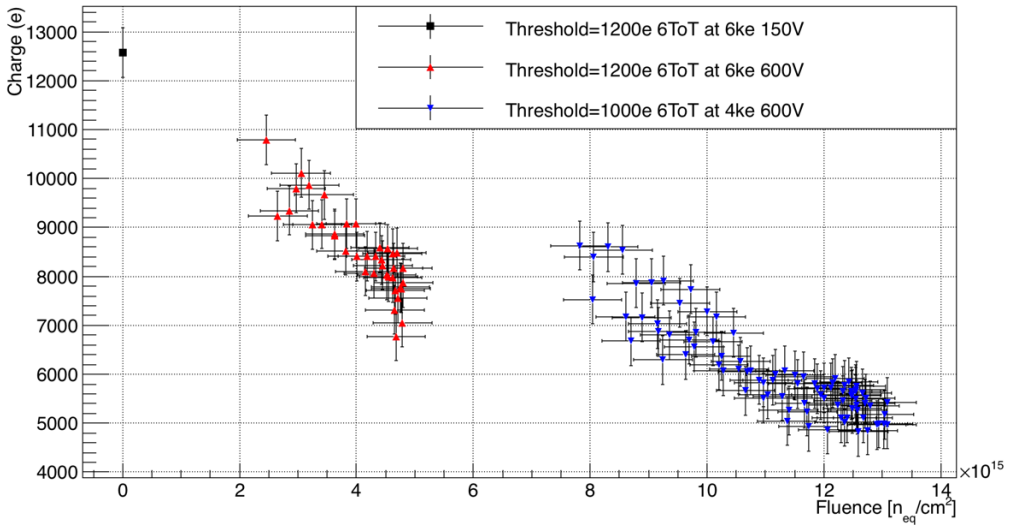

Figure 14: Collected charge vs Fluence for two sets of tuning: Threshold=1200e, 6ToT at 6ke (150 V bias voltage, un-irradiated and 600 V bias voltage, irradiated) and Threshold=1000e, 6ToT at 4ke, 600 V bias voltage.

charge is steeper at lower fluences (red markers) than at higher fluences (blue markers). This is probably due to a threshold tuning of poorer quality of the former with respect to the latter. It can also be seen that the collected charge at the highest tested fluence ($\Phi = 1.3 \times 10^{16} \mathrm{n_{eq}/cm^2}$) is greater than 4000 e at 600 V.

From Figure 14 the charge collection efficiency (CCE) was derived. The charge value before irradiation was obtained from the W30 sensor (100 μm thick). For the other fluences, the charge reported in Figure 14 was obtained from the W80 sensor (130 μm thick). Consequently the normalisation for the irradiated module was 1.3 times higher than for the un-irradiated one.

Figure 15 shows the CCE of W80 over a typical ITk like fluence range. The distribution is fitted with the Hecht function ([30]; see also Appendix A in [31]). From these fits the effective trapping constant β can be extracted; as a first approximation β was assumed to be equal for holes and electrons. For the intermediate fluence dataset (red triangles) the following value for the trapping constant was extracted: $\beta = 5.3 \pm 0.2 \times 10^{-16}$ cm^2/ns; for the higher fluence dataset (blue triangles) a value of $\beta = 3.5 \pm 0.1 \times 10^{-16}$ cm^2/ns was fitted. The two values are of the same order of magnitude, their differences

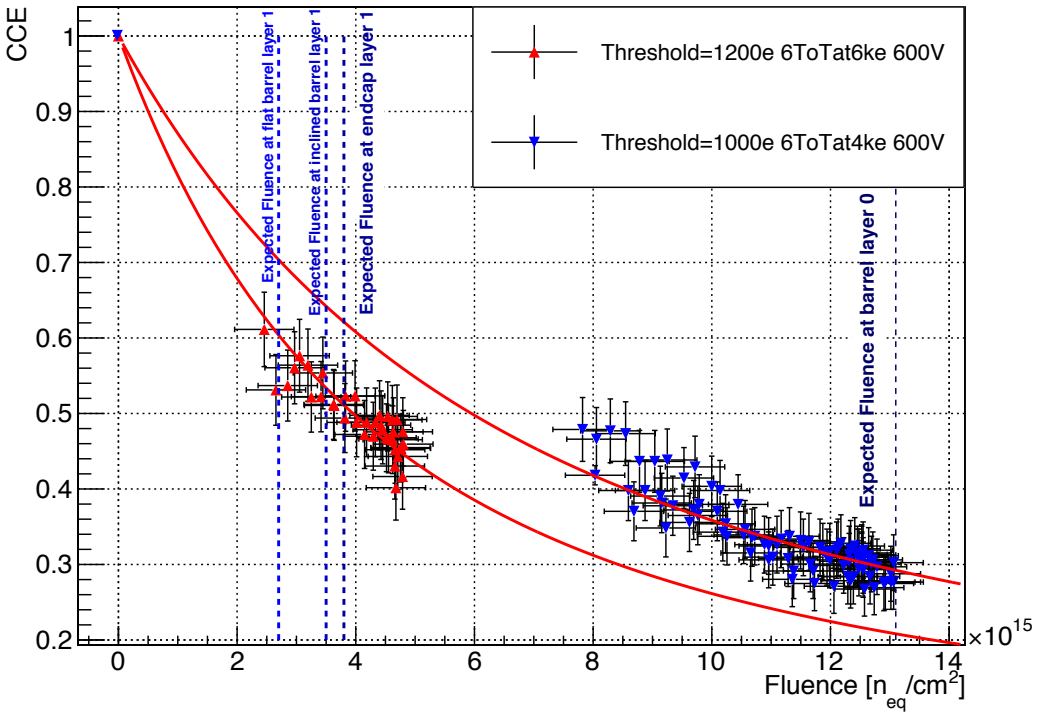

Figure 15: Charge collection efficiency (CCE) measurement for two sets of tuning: Threshold=1200e, 6ToT at 6000e and Threshold=1000e, 6ToT at 4000e. Expected end-of-lifetime fluences for ITk are also indicated. Data were collected at 600 V bias voltage. Red line is a fit on data.

come from the different tuning configurations, from a different annealing time or from the various approximations used. The fitted values reported here are somewhat smaller than those listed in Ref. [32] (4-6 $\times 10^{-16}$ cm^2/ns); this can be in part explained by the fact that the Hecht formula used to fit data assumes a mono-dimensional detector (*i.e.* a pad detector whose sides are much larger than its thickness); the limitations of FE-I4 chip have also an impact. Hence the β values obtained are to be considered as lower limits for the true ones.

The 4 vertical blue dotted lines represents the expected fluences at the end of lifetime of 4 different layers of ITk [7] (see list in Section 4.3). The Table 5 compiles the values of the intersections of the 2 fits with the 4 fluence lines.

For the 1000 electrons threshold and the three fluences corresponding to the accumulated dose at layer 1, the charge collection efficiency is higher than

Table 5: Charge collection efficiency for two tunings over the ITk fluence range.

Calibration	Fluences ($\Phi = 1 \times 10^{15} n_{eq}/cm^2$)			
	2.7	3.5	3.8	13.1
Thr.=1200e, 6ToT at 6000e, CCE =	61%	53%	51%	21%
Thr.=1000e, 6ToT at 4000e, CCE =	71%	64%	62%	29%

60%. At $\Phi = 1.3 \times 10^{16} n_{eq}/cm^2$, the fluence expected at Layer 0 in the flat section after 2000 fb^{-1}, the charge collection efficiency is lower than 30%.

5. Conclusions

Planar pixels sensors produced at FBK Trento by LPNHE and INFN were tested in beam before and after irradiation to fluences comparable to those expected at the end of the HL-LHC. Results indicate that the detectors meet all the specifications of the ATLAS ITk for all but the very innermost pixel layers; in particular hit efficiency is as high as 97% for fluences up to to $\Phi = 7 \times 10^{15} n_{eq}/cm^2$. Collected data allowed also the estimation of the trapping constant, even if the accuracy is limited by pixel geometry modelling and the FE-I4 chip performance. A new pixel production at FBK is completed and detector prototypes are being measured; the available sensors are 100 μm thick and compatible with the new readout chip for the ITk pixels modules (RD53A [13]).

Acknowledgments

Planar pixel production presented in this paper are supported by the Italian National Institute for Nuclear Research (INFN), Projects ATLAS, CMS, RD-FASE2 (CSN1) and by the H2020 project AIDA-2020, GA no. 654168. Some of the measurements leading to these results have been performed at the Test Beam Facility at DESY Hamburg (Germany), a member of the Helmholtz Association (HGF). The authors want to thanks the CERN IRRAD team for helping with the irradiation of the sensors and everyone involved in the support of the testbeam activity in the CERN North Area Test Beam Facility for making some of the measurements presented here possible.

References

[1] The HL-LHC project.
URL http://hilumilhc.web.cern.ch/about/hl-lhc-project

[2] ATLAS Collaboration, The ATLAS Experiment at the CERN Large Hadron Collider, JINST 3 (2008) S08003. doi:10.1088/1748-0221/3/08/S08003.

[3] ATLAS collaboration, Inner detector - technical design report, 1, Tech. rep., CERN (1997).
URL http://cdsweb.cern.ch/record/331063

[4] ATLAS collaboration, Inner detector - technical design report, 2, Tech. rep., CERN (1997).
URL http://cdsweb.cern.ch/record/381263

[5] S. McMahon, P. Allport, H. Hayward, B. Di Girolamo, Initial Design Report of the ITk: Initial Design Report of the ITk, Tech. Rep. ATL-COM-UPGRADE-2014-029, CERN, Geneva (Oct 2014).
URL https://cds.cern.ch/record/1952548

[6] Technical Design Report for the ATLAS Inner Tracker Strip Detector (Apr 2017).
URL https://cds.cern.ch/record/2257755

[7] ATLAS Collaboration, Technical Design Report for the ATLAS Inner Tracker Pixel Detector, Tech. Rep. CERN-LHCC-2017-021. ATLAS-TDR-030, CERN, Geneva (Sep 2017).
URL https://cds.cern.ch/record/2285585

[8] M. Capeans, G. Darbo, K. Einsweiller, M. Elsing, T. Flick, M. Garcia-Sciveres, C. Gemme, H. Pernegger, O. Rohne, R. Vuillermet, ATLAS Insertable B-Layer Technical Design Report, Tech. Rep. CERN-LHCC-2010-013. ATLAS-TDR-19, CERN (Sep 2010).
URL https://cds.cern.ch/record/1291633

[9] B. Abbott, et al., Production and Integration of the ATLAS Insertable B-Layer, JINST 13 (05) (2018) T05008. doi:10.1088/1748-0221/13/05/T05008.

[10] G. Kramberger, V. Cindro, I. Mandič, M. Mikuž, M. Zavrtanik, Effective trapping time of electrons and holes in different silicon materials irradiated with neutrons, protons and pions, Nucl. Instr. and Meth. A 481 (1) (2002) 297 – 305. doi:10.1016/S0168-9002(01)01263-3.

[11] G.-F. D. Betta, M. Boscardin, M. Bomben, M. Brianzi, G. Calderini, G. Darbo, R. Dell'Orso, A. Gaudiello, G. Giacomini, R. Mendicino, M. Meschini, A. Messineo, S. Ronchin, D. Sultan, N. Zorzi, The infn-fbk "phase-2" r&d program, Nucl. Instr. and Meth. A 824 (2016) 388 – 391, frontier Detectors for Frontier Physics: Proceedings of the 13th Pisa Meeting on Advanced Detectors. doi:10.1016/j.nima.2015.08.074.

[12] M. Garcia-Sciveres, et al., The FE-I4 pixel readout integrated circuit, Nucl. Instrum. Meth. A636 (2011) S155–S159. doi:10.1016/j.nima.2010.04.101.

[13] RD53 Collaboration.
URL https://rd53.web.cern.ch/RD53/

[14] H. C. Kastli, M. Barbero, W. Erdmann, C. Hormann, R. Horisberger, D. Kotlinski, B. Meier, Design and performance of the CMS pixel detector readout chip, Nucl. Instrum. Meth. A565 (2006) 188–194. doi:10.1016/j.nima.2006.05.038.

[15] M. Bomben, A. Ducourthial, et al., Performance of active edge pixel sensors, JINST 12 (05) (2017) P05006. doi:10.1088/1748-0221/12/05/P05006.

[16] E. Vianello, A. Bagolini, P. Bellutti, M. Boscardin, G.-F. Betta, G. Giacomini, C. Piemonte, M. Povoli, N. Zorzi, Optimization of double-side 3d detector technology for first productions at fbk, in: Nuclear Science Symposium and Medical Imaging Conference (NSS/MIC), 2011 IEEE, 2011, pp. 523–528. doi:10.1109/NSSMIC.2011.6154102.

[17] S. Terzo, Development of radiation hard pixel modules employing planar n-in-p silicon sensors with active edges for the atlas detector at hl-lhc, Ph.D. thesis, Technische Universitat Munchen, Max-Planck-Institut fur Physik (2015).
URL https://mediatum.ub.tum.de/doc/1276352/1276352.pdf

[18] Y. Unno, et al., Development of novel n+-in-p silicon planar pixel sensors for hl-lhc, Nucl. Instrum. Meth. A699 (2013) 72 – 77. doi:10.1016/j.nima.2012.04.061.

[19] M. Moll, Radiation damage in silicon particle detectors: Microscopic defects and macroscopic properties, Ph.D. thesis, Hamburg U. (1999). URL http://www-library.desy.de/cgi-bin/showprep.pl?desy-thesis99-040

[20] A. Chilingarov, Temperature dependence of the current generated in si bulk, Journal of Instrumentation 8 (10) (2013) P10003. doi:10.1088/1748-0221/8/10/P10003.

[21] N. Savic, J. Beyer, A. Macchiolo, R. Nisius, Investigation of thin n-in-p planar pixel modules for the ATLAS upgrade, JINST 11 (12) (2016) C12008. doi:10.1088/1748-0221/11/12/C12008.

[22] S. Jansen, H. Spannagel et al, Performance of the eudet-type beam telescopes, EPJ Techniques and Instrumentation 3 (1) (2016) 7. doi:10.1140/epjti/s40485-016-0033-2.

[23] J. Weingarten, S. Altenheiner, M. Beimforde, M. Benoit, M. Bomben, et al., Planar Pixel Sensors for the ATLAS Upgrade: Beam Tests results, JINST 7 (2012) P10028. doi:10.1088/1748-0221/7/10/P10028.

[24] C. Hu-Guo, et al., First reticule size {MAPS} with digital output and integrated zero suppression for the eudet-jra1 beam telescope, Nucl. Instr. and Meth. A 623 (1) (2010) 480 – 482, 1st International Conference on Technology and Instrumentation in Particle Physics. doi:10.1016/j.nima.2010.03.043.

[25] http://eutelescope.web.cern.ch/.
URL http://eutelescope.web.cern.ch/

[26] https://bitbucket.org/TBmon2/tbmon2/overview.
URL https://bitbucket.org/TBmon2/tbmon2/overview

[27] S. Parker, C. Kenney, J. Segal, 3d - a proposed new architecture for solid-state radiation detectors, Nucl. Instr. and Meth. A 395 (3) (1997) 328 – 343. doi:10.1016/S0168-9002(97)00694-3.

[28] A. Ducourthial, et al., Thin and edgeless sensors for ATLAS pixel detector upgrade, JINST 12 (12) (2017) C12038. doi:10.1088/1748-0221/12/12/C12038.

[29] M. Backhaus, et al., Development of a versatile and modular test system for ATLAS hybrid pixel detectors, Nucl. Instr. Meth. A 650 (1) (2011) 37 – 40, international Workshop on Semiconductor Pixel Detectors for Particles and Imaging 2010. doi:10.1016/j.nima.2010.12.087.

[30] K. Hecht, Zum Mechanismus des lichtelektrischen Primärstromes in isolierenden Kristallen, Zeit. Physik. (1932) 77:235.

[31] M. Bomben, Silicon Trackers for High Luminosity Colliders, Habilitation à diriger des recherches, Université Paris Diderot (Paris 7) Sorbonne Paris Cité (Mar. 2018).
URL https://tel.archives-ouvertes.fr/tel-01824535

[32] G. Kramberger, et al., Effective trapping time of electrons and holes in different silicon materials irradiated with neutrons, protons and pions, Nucl. Instr. and Meth. A 481 (1-3) (2002) 297 – 305. doi:10.1016/S0168-9002(01)01263-3.